CHAPTER IV
RESULTS AND DISCUSSION

4.1 Adsorbents Characterization

4.1.1 Characterization of Adsorbent by Nitrogen Adsorption/Desorption Method and Mercury Porosimetry

The different adsorbents (mesoporous and macroporous alumina : m-Al_2O_3 and M-Al_2O_3, plus activated carbon: AC) were characterized by using Nitrogen adsorption/desorption at 77K and Mercury porosimetry methods, to study the properties of the porosity, porous structure and surface area which are presented in Tables 4.1 and 4.2.

Table 4.1 Properties of adsorbents by using the Nitrogen adsorption / desorption method at 77K

Adsorbents (IFP Reference)	Properties				
	B.E.T. Surface Area (m^2/g)	V_μ (t-plot) (cm^3/g)	V_m (B.J.H.-desorption) (cm^3/g)	$V_m + V_\mu$ (P/P_0=0.99) (cm^3/g)	V_m (cm^3/g)
Macroporous Alumina (70337)	194	0.000	0.552	0.523	0.523
Small particle of M-Al_2O_3 at diameter size 300-500 μm (87257)	194	0.000	0.557	0.525	0.525
100% monolayer of $CuCl_2$ on M-Al_2O_3 (84451)	158	0.000	0.432	0.412	0.412
75% monolayer of $CuCl_2$ on M-Al_2O_3 (84452)	164	0.000	0.448	0.429	0.429
50% monolayer of $CuCl_2$ on M-Al_2O_3 (84453)	178	0.000	0.494	0.469	0.469

Table 4.1 (Cont.) Properties of adsorbents by using the Nitrogen adsorption / desorption method at 77K

Adsorbents (IFP Reference)	Properties				
	B.E.T. Surface Area (m^2/g)	V_μ (t-plot) (cm^3/g)	V_m (B.J.H.-desorption) (cm^3/g)	$V_m + V_\mu$ (P/P_0=0.99) (cm^3/g)	V_m (cm^3/g)
100% monolayer of $NiCl_2$ on M-Al_2O_3 (84454)	178	0.000	0.484	0.457	0.457
75% monolayer of $NiCl_2$ on M-Al_2O_3 (84455)	182	0.000	0.500	0.472	0.472
50% monolayer of $NiCl_2$ on M-Al_2O_3 (84456)	183	0.000	0.511	0.482	0.482
Mesoporous Alumina (70333)	278	0.000	0.797	0.752	0.752
Small particle of m-Al_2O_3 at diameter size 300-500 μm (87258)	292	0.000	0.795	0.743	0.743
100% monolayer of $CuCl_2$ on m-Al_2O_3 (84457)	218	0.000	0.575	0.545	0.545
75% monolayer of $CuCl_2$ on m-Al_2O_3 (84458)	228	0.000	0.623	0.589	0.589
50% monolayer of $CuCl_2$ on m-Al_2O_3 (84459)	246	0.000	0.672	0.637	0.637
100% monolayer of $NiCl_2$ on m-Al_2O_3 (84460)	247	0.000	0.669	0.630	0.630
75% monolayer of $NiCl_2$ on m-Al_2O_3 (84461)	262	0.000	0.696	0.661	0.661
50% monolayer of $NiCl_2$ on m-Al_2O_3 (84462)	291	0.000	0.761	0.719	0.719

Table 4.1 (Cont.) Properties of adsorbents by using the Nitrogen adsorption / desorption method at 77K

Adsorbents (IFP Reference)	Properties				
	B.E.T. Surface Area (m^2/g)	V_μ (t-plot) (cm^3/g)	V_m (B.J.H.-desorption) (cm^3/g)	$V_m + V_\mu$ (P/P_0=0.99) (cm^3/g)	V_m (cm^3/g)
Crushed before impregnation at diameter size 300-500 µm 100% monolayer of $CuCl_2$ on m-Al_2O_3 (85287)	242	0.000	0.582	0.555	0.555
Crushed before impregnation at diameter size 300-500 µm 75% monolayer of $CuCl_2$ on m-Al_2O_3 (85289)	249	0.000	0.614	0.583	0.583
Crushed before impregnation at diameter size 300-500 µm 50% monolayer of $CuCl_2$ on m-Al_2O_3 (85290)	257	0.000	0.660	0.622	0.622
Crushed *after* impregnation at diameter size 300-500 µm 100% monolayer of $CuCl_2$ on m-Al_2O_3 (87260)	220	0.000	0.569	0.545	0.545
Crushed *after* impregnation at diameter size 300-500 µm 75% monolayer of $CuCl_2$ on m-Al_2O_3 (87261)	240	0.000	0.618	0.591	0.591
Crushed *after* impregnation at diameter size 300-500 µm 50% monolayer of $CuCl_2$ on m-Al_2O_3 (87262)	252	0.000	0.670	0.638	0.638

Table 4.1 (Cont.) Properties of adsorbents by using the Nitrogen adsorption / desorption method at 77K

Adsorbents (IFP Reference)	Properties				
	B.E.T. Surface Area (m^2/g)	V_μ (t-plot) (cm^3/g)	V_m (B.J.H.-desorption) (cm^3/g)	$V_m + V_\mu$ (P/P_0=0.99) (cm^3/g)	V_m (cm^3/g)
AC (75192)	929	0.265	0.295	0.621	0.356
43% wt of $CuCl_2$ on AC (87411)	844	0.247	0.272	0.573	0.326

Table 4.2 Properties of adsorbents by using the Mercury porosimetry

Adsorbents	Properties				
	Particle Density (g/cm^3)	Structural Density (g/cm^3)	V_m (cm^3/g)	V_M (cm^3/g)	V_m+V_M (cm^3/g)
Macroporous Alumina (70337)	1.008	2.994	0.481	0.151	0.632
Small particle of M-Al_2O_3 at diameter size 300-500 µm (87257)	0.5464	2.396	0.470	0.110	0.580
100% monolayer of $CuCl_2$ on M-Al_2O_3 (84451)	1.187	3.387	0.397	0.130	0.527
75% monolayer of $CuCl_2$ on M-Al_2O_3 (84452)	1.124	3.300	0.430	0.137	0.567
50% monolayer of $CuCl_2$ on M-Al_2O_3 (84453)	1.053	2.952	0.447	0.144	0.591
100% monolayer of $NiCl_2$ on M-Al_2O_3 (84454)	1.0962	2.976	0.408	0.144	0.552
75% monolayer of $NiCl_2$ on M-Al_2O_3 (84455)	1.0635	2.984	0.438	0.147	0.585
50% monolayer of $NiCl_2$ on M-Al_2O_3 (84456)	1.0237	2.750	0.446	0.147	0.593
Mesoporous Alumina (70333)	0.914	2.806	0.643	0.009	0.652

Table 4.2 (Cont.) Properties of adsorbents by using the Mercury porosimetry

Adsorbents	Properties				
	Particle Density (g/cm^3)	Structural Density (g/cm^3)	V_m (cm^3/g)	V_M (cm^3/g)	V_m+V_M (cm^3/g)
Small particle of m-Al_2O_3 at diameter size 300-500 μm (87258)	0.519	2.715	0.660	0.019	0.679
100% monolayer of $CuCl_2$ on m-Al_2O_3 (84457)	1.096	3.052	0.488	0.014	0.502
75% monolayer of $CuCl_2$ on m-Al_2O_3 (84458)	1.080	2.982	0.523	0.017	0.540
50% monolayer of $CuCl_2$ on m-Al_2O_3 (84459)	1.069	3.208	0.564	0.020	0.584
100% monolayer of $NiCl_2$ on m-Al_2O_3 (84460)	1.077	2.800	0.504	0.006	0.510
75% monolayer of $NiCl_2$ on m-Al_2O_3 (84461)	1.008	2.744	0.544	0.006	0.550
50% monolayer of $NiCl_2$ on m-Al_2O_3 (84462)	0.940	2.450	0.565	0.011	0.576
Crushed before impregnation at diameter size 300-500 μm 100% monolayer of $CuCl_2$ on m-Al_2O_3 (85287)	0.695	2.848	0.460	0.023	0.483
Crushed before impregnation at diameter size 300-500 μm 75% monolayer of $CuCl_2$ on m-Al_2O_3 (85289)	0.615	2.894	0.530	0.031	0.561
Crushed before impregnation at diameter size 300-500 μm 50% monolayer of $CuCl_2$ on m-Al_2O_3 (85290)	0.617	2.759	0.538	0.033	0.571

Table 4.2 (Cont.) Properties of adsorbents by using the Mercury porosimetry

Adsorbents	Properties				
	Particle Density (g/cm^3)	Structural Density (g/cm^3)	V_m (cm^3/g)	V_M (cm^3/g)	V_m+V_M (cm^3/g)
Crushed *after* impregnation at diameter size 300-500 μm 100% monolayer of $CuCl_2$ on m-Al_2O_3 (87260)	0.646	3.085	0.459	0.013	0.472
Crushed *after* impregnation at diameter size 300-500 μm 75% monolayer of $CuCl_2$ on m-Al_2O_3 (87261)	0.684	2.853	0.509	0.013	0.522
Crushed *after* impregnation at diameter size 300-500 μm 50% monolayer of $CuCl_2$ on m-Al_2O_3 (87262)	0.584	2.766	0.555	0.015	0.570
Activated Carbon (75192)	0.367	0.520	0.220	0.446	0.666
43% wt of $CuCl_2$ on AC (87411)	0.609	1.250	0.247	0.466	0.713

Where V_μ = microporous volume,

V_m = mesoporous volume

V_M = macroporous volume

According to Table 4.1, activated carbon has the highest B.E.T. surface area followed by m-Al_2O_3 and M-Al_2O_3 respectively, and since the metal, Cu^{2+}, covers the surface of the adsorbent, the surface area is decreased. For the porous volume, it was determined that there are no micropores for alumina based adsorbents, and for the mesoporous volume, m-Al_2O_3 has the highest one followed by M-Al_2O_3 and activated carbon respectively. The greater is the metal loading, the lower is the mesoporous volume which corresponds to the decrease of surface area.

From Table 4.2, M-Al_2O_3 has the highest particle density following by m-Al_2O_3 and activated carbon respectively and for both of M-Al_2O_3 and m-Al_2O_3, the particle density is increased when impregnated with more metal. For the mesoporous volume determined with mercury intrusion, it shows the same tendency as the result from Nitrogen adsorption/desorption methods: m-Al_2O_3 has the highest mesoporous volume followed by M-Al_2O_3 and activated carbon respectively. For macroporous volume, activated carbon has the highest macroporous volume followed by M-Al_2O_3 and m-Al_2O_3 respectively.

4.1.2 Temperature-Programmed Reduction of $CuCl_2$ Impregnated on the Adsorbent

After impregnation, Cu^{2+} impregnated on the adsorbent has to be reduced to Cu^{+}. Thus, to find the effective conditions for reduction, TPR was used. $CuCl_2$ impregnated on M-Al_2O_3 was first heated in a flow 10% H_2 in Ar up to 900 °C at a heating rate of 5 °C/min. The intensity measured by thermal conductivity detector (TCD) indicates H_2 consumption.

The result with different percent monolayer of metal loading impregnated on m-Al_2O_3 and M-Al_2O_3 are shown in Figures 4.1-4.4, and 4.5 to 4.8, respectively.

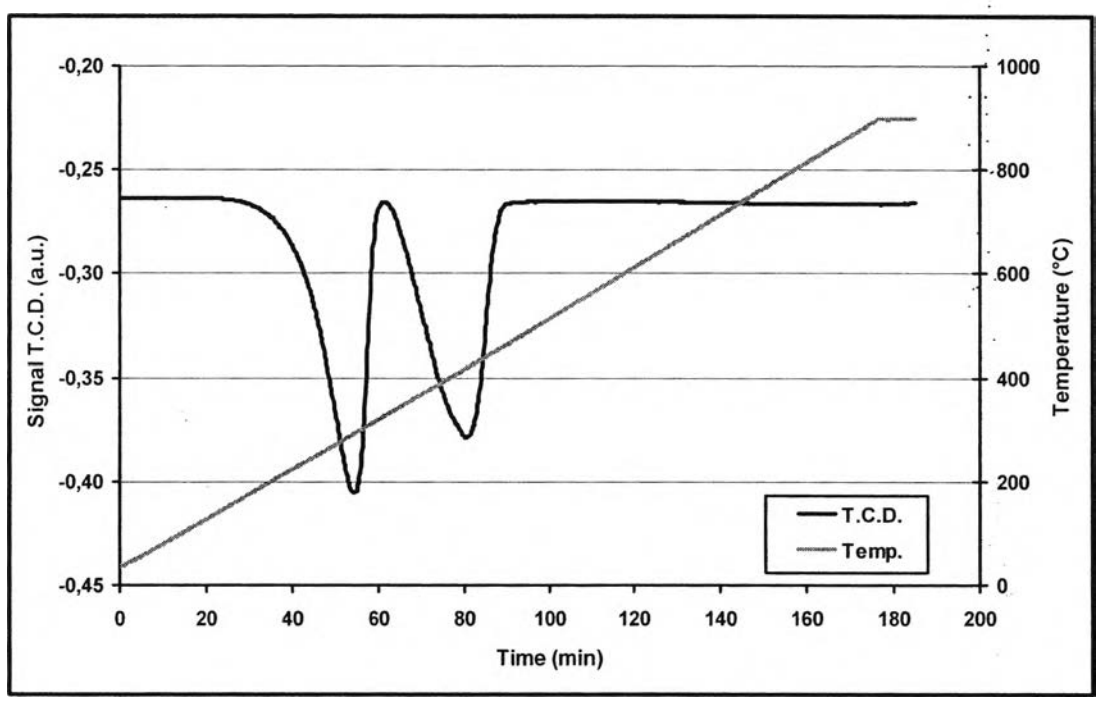

Figure 4.1 Temperature-programmed reduction (TPR) of 100% monolayer of $CuCl_2$ impregnated on M-Al_2O_3 in 10% H_2 in Ar.

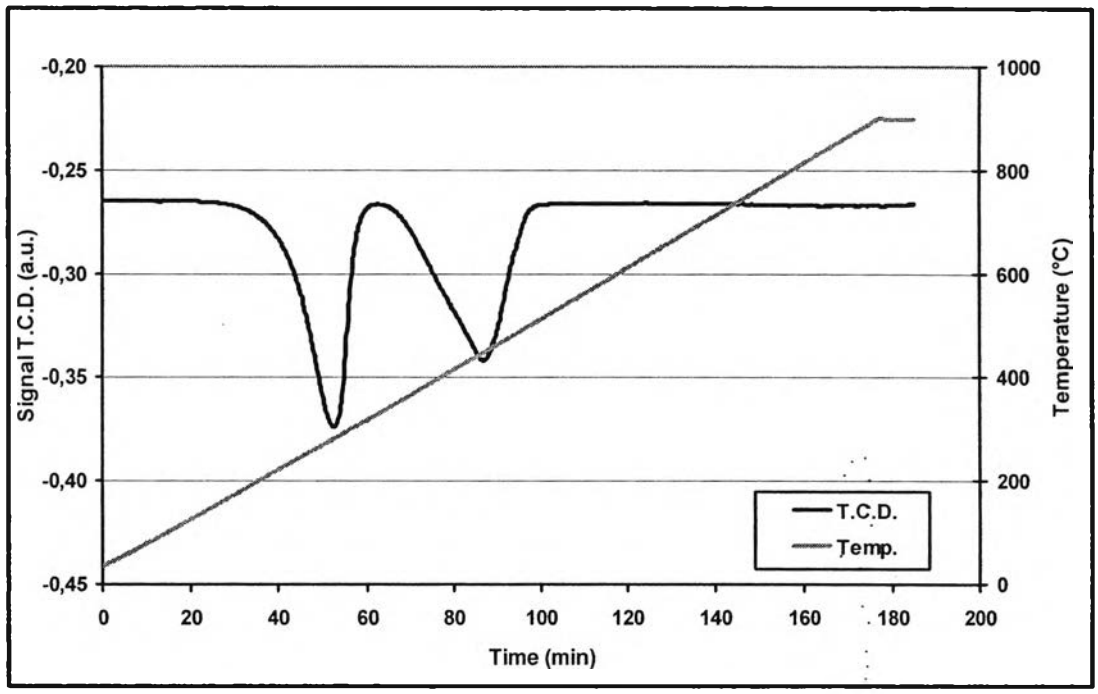

Figure 4.2 Temperature-programmed reduction (TPR) of 75% monolayer of $CuCl_2$ impregnated on M-Al_2O_3 in 10% H_2 in Ar.

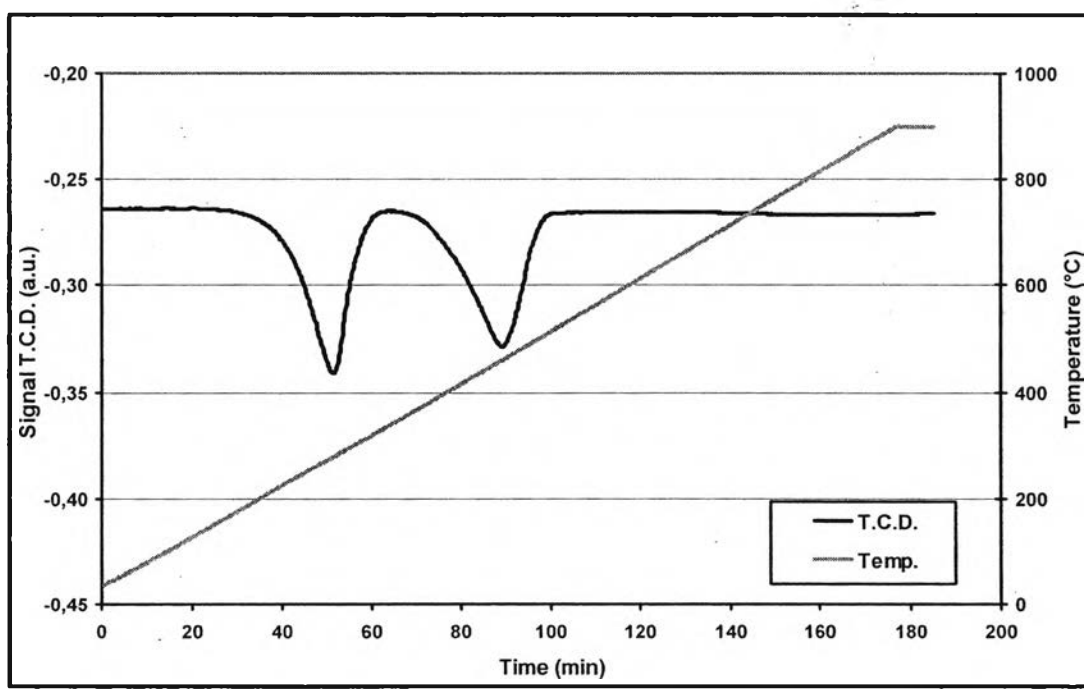

Figure 4.3 Temperature-programmed reduction (TPR) of 50% monolayer of $CuCl_2$ impregnated on M-Al_2O_3 in 10% H_2 in Ar.

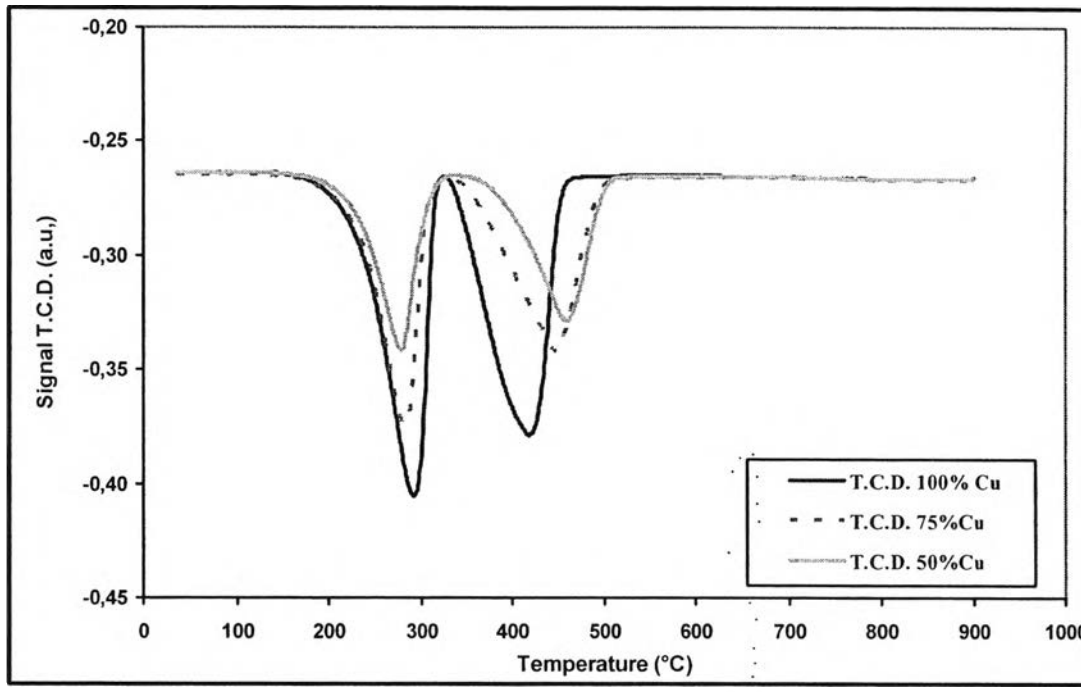

Figure 4.4 Summary curve of temperature-programmed reduction (TPR) of 100%, 75% and 50% monolayer of $CuCl_2$ impregnated on M-Al_2O_3 in 10% H_2 in Ar.

Table 4.3 Reduction temperature of 100%, 75% and 50% monolayer of $CuCl_2$ impregnated on M-Al_2O_3

Adsorbent	Peak Number	Temperature (°C)
100% monolayer of $CuCl_2$ on M-Al_2O_3 (Figure 4.1)	1 2	292 417
75% monolayer of $CuCl_2$ on M-Al_2O_3 (Figure 4.2)	1 2	282 447
50% monolayer of $CuCl_2$ on M-Al_2O_3 (Figure 4.3)	1 2	279 459

From Figures 4.1 – 4.3, it can be seen the results of 100%, 75% and 50% monolayer of $CuCl_2$ impregnated on M-Al_2O_3, during the heat treatment of $CuCl_2$ in H_2. Two distinct peaks were detected as shown in Table 4.3, which correspond to two reduction steps. The first peak at the lowest temperature indicated the reduction from Cu^{2+} to Cu^{+}, and the second peak at the highest temperature indicated the reduction from Cu^{+} to Cu^{0}. From Table 4.3, the temperature at the first peak is the appropriate temperature to reduce Cu^{2+} to Cu^{+} which is around 280-290 °C. The above results indicate that almost 100% of Cu^{2+} has been reduced at 290 °C for 60 minutes in presence of H_2.

From Figure 4.4, the peak area of 100% monolayer of $CuCl_2$ impregnated on M-Al_2O_3 is higher than 75% and 50% monolayer of $CuCl_2$ impregnated on M-Al_2O_3 respectively which corresponds to the amount of metal impregnated on the adsorbent. Moreover, for the Cu^{+} on M-Al_2O_3, the temperature at the second peak was increased in order of 50% monolayer of $CuCl_2$ > 75% monolayer of $CuCl_2$ > 100% monolayer of $CuCl_2$, indicating that the interaction between the metal and the adsorbent was higher at the lower amount of metal loading.

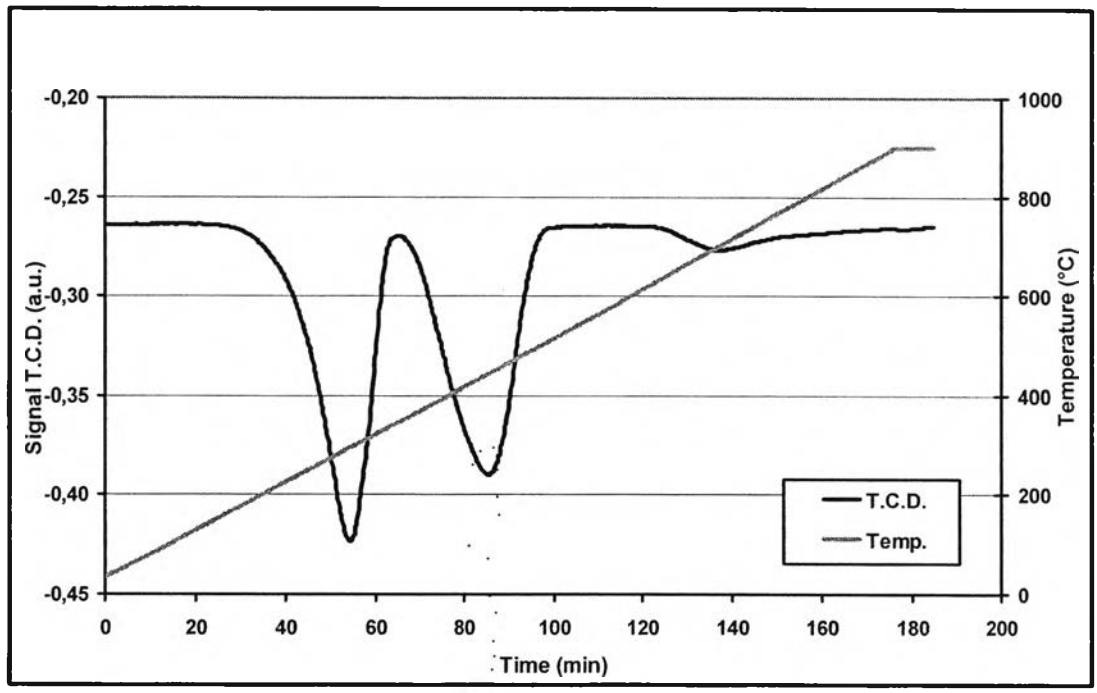

Figure 4.5 Temperature-programmed reduction (TPR) of 100% monolayer of $CuCl_2$ impregnated on m-Al_2O_3 in 10% H_2 in Ar.

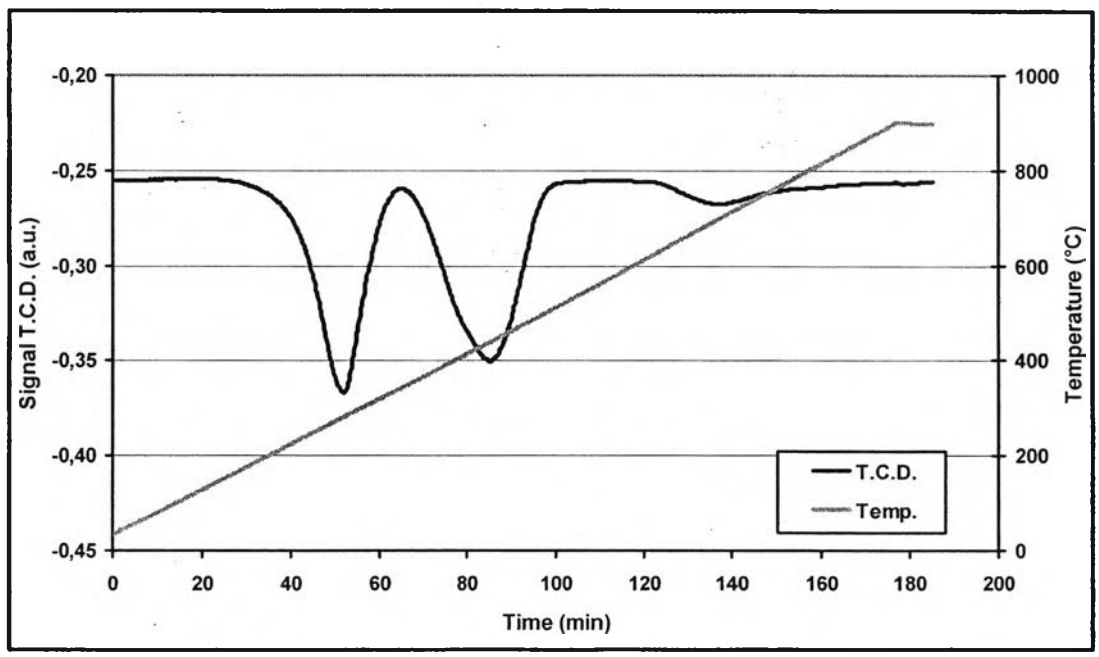

Figure 4.6 Temperature-programmed reduction (TPR) of 75% monolayer of $CuCl_2$ impregnated m-Al_2O_3 in 10% H_2 in Ar.

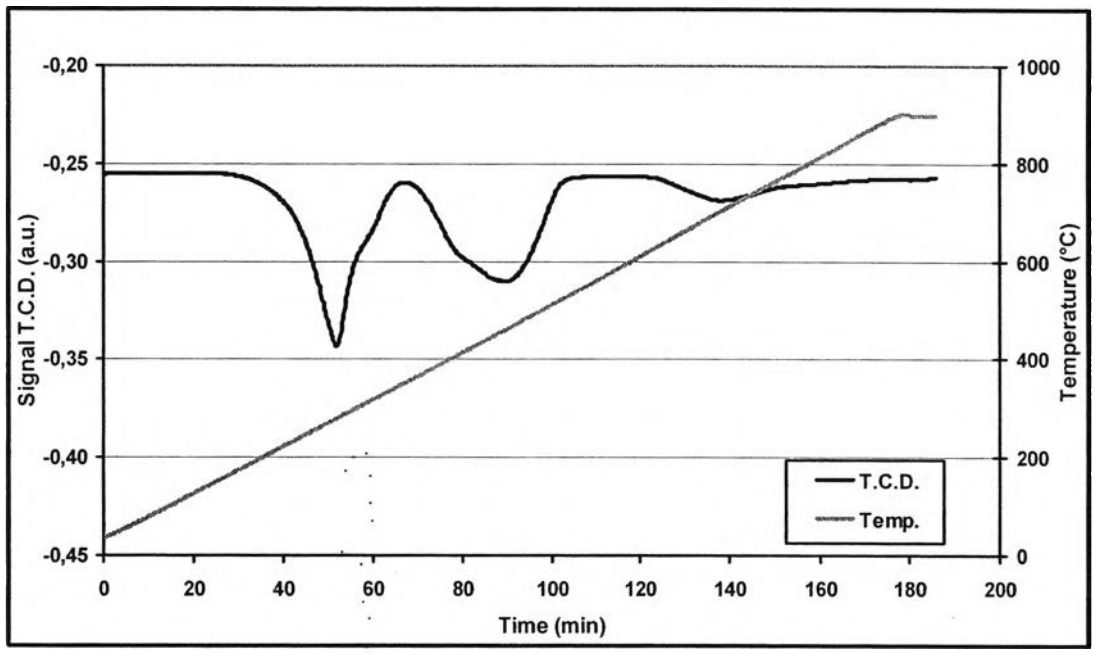

Figure 4.7 Temperature-programmed reduction (TPR) of 50% monolayer of $CuCl_2$ impregnated on m-Al_2O_3 in 10% H_2 in Ar.

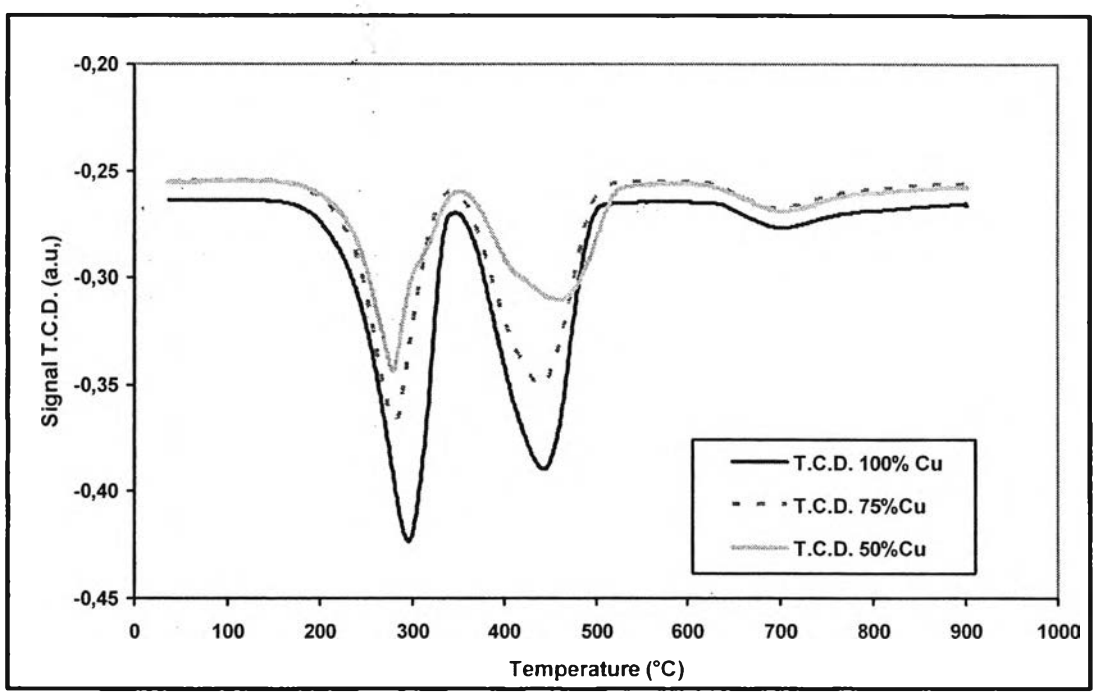

Figure 4.8 Summary curve of temperature-programmed reduction (TPR) of 100%, 75% and 50% monolayer of $CuCl_2$ impregnated on m-Al_2O_3 in 10% H_2 in Ar.

Table 4.4 Reduction temperature of 100%, 75% and 50% monolayer of $CuCl_2$ impregnated on m-Al_2O_3

Adsorbent	Peak Number	Temperature (°C)
100% monolayer of $CuCl_2$ on m-Al_2O_3 (Figure 4.5)	1	295
	2	443
	3	700
75% monolayer of $CuCl_2$ on m-Al_2O_3 (Figure 4.6)	1	281
	2	434
	3	699
50% monolayer of $CuCl_2$ on m-Al_2O_3 (Figure 4.7)	1	279
	2	458
	3	704

From Figures 4.5 – 4.7, it can be seen the result of 100%, 75% and 50% monolayer of $CuCl_2$ impregnated on m-Al_2O_3, during the heat treatment of $CuCl_2$ in H_2. Two main distinct peaks plus another small one were detected as shown in Table 4.4, which corresponds to two reduction steps. The first peak indicated the reduction from Cu^{2+} to Cu^{+}, and the second peak indicated the reduction from Cu^{+} to Cu^{0}, but for third peak, it was detected around 700 °C which is not an effect of the reduction. So it could be interesting to study about the morphology of m-Al_2O_3 which changed at the high temperature to another type of alumina. From Table 4.4, the temperature at the first peak is the appropriate temperature to reduce to Cu^{+} which is around 280-290 °C. The above results indicate that almost 100% of Cu^{2+} has been reduced into Cu^{+} at around 290 °C for 60 minutes in presence of H_2. The results are similar for both mesoporous and macroporous alumina adsorbent.

From Figure 4.8, the peak area of 100% monolayer of $CuCl_2$ impregnated on m-Al_2O_3 is higher than 75% and 50% monolayer of $CuCl_2$ impregnated on m-Al_2O_3 respectively, which corresponds to the amount of metal impregnated on the adsorbent. The peak area of m-Al_2O_3 adsorbents is higher than M-Al_2O_3 adsorbents which correspond to the grater surface area.

Table 4.5 Hydrogen consumption of adsorbent

Adsorbent	H_2 consumption (mmol/g)			Amount of $CuCl_2$ (mmol/g adsorbent)
	Peak No.1	Peak No.2	Sum 1+2	
100% monolayer of $CuCl_2$ on M-Al_2O_3	0.707	0.801	1.508	1.426
75% monolayer of $CuCl_2$ on M-Al_2O_3	0.510	0.583	1.093	1.179
50% monolayer of $CuCl_2$ on M-Al_2O_3	0.361	0.458	0.819	0.828
100% monolayer of $CuCl_2$ on m-Al_2O_3	0.905	0.885	1.790	1.967
75% monolayer of $CuCl_2$ on m-Al_2O_3	0.616	0.732	1.349	1.578
50% monolayer of $CuCl_2$ on m-Al_2O_3	0.462	0.499	0.961	1.129

From Table 4.5, hydrogen consumption of all adsorbents are shown, the amount of $CuCl_2$ was calculated from preparation step, the result shown that the amount of hydrogen consumption was similar to the amount of $CuCl_2$ that corresponds to 1 mole of H_2 reacting with 1 mole of $CuCl_2$. It can be interpreted in chemical equation as follow:

$$CuCl_2 + \frac{1}{2}H_2 \rightarrow CuCl + HCl \quad (4.1)$$

$$CuCl + \frac{1}{2}H_2 \rightarrow Cu + HCl \quad (4.2)$$

$$CuCl_2 + H_2 \rightarrow Cu + 2HCl \quad (4.3)$$

4.1.3 Scanning Electron Microscope (SEM)

The porosity and the metal dispersion within the adsorbents were studied by using SEM. The adsorbent was first included into resin, then cutted at the cross section to study at the internal surface.

The image of non-impregnated macroporous alumina (M-Al_2O_3) presented in Fig.4.9 (a) showed a higher porosity than 100 % monolayer of $CuCl_2$/M-Al_2O_3 in Fig.4.9 (b) which corresponds to the result from N_2 adsorption/desorption method and Mercury porosimetry. Fig.4.9 (c) presents the cross section of 100 % monolayer of $CuCl_2$/M-Al_2O_3 showing agglomerates of $CuCl_2$ in some position. So the impregnation method succeed to add the metal inside the pores of the solid, nevertheless, the impregnation seemed to be not homogeneous.

The images of non-impregnated m-Al_2O_3 and 100 % monolayer of $CuCl_2$/m-Al_2O_3, shown in Fig.4.9 (d), (e) and (f), led to similar results to M-Al_2O_3 based adsorbents. The non-impregnated mesporous alumina (m-Al_2O_3) has a higher porosity than the impregnated one, and the agglomerates of $CuCl_2$ was also found in the some position.

Fig.4.10 (a) and (b) show the images of small particle of 100% monolayer of $CuCl_2$/m-Al_2O_3 crushed before impregnation at diameter size 300-500 μm, $CuCl_2$ seemed to cover essentially the external surface with more than a monolayer coverage.

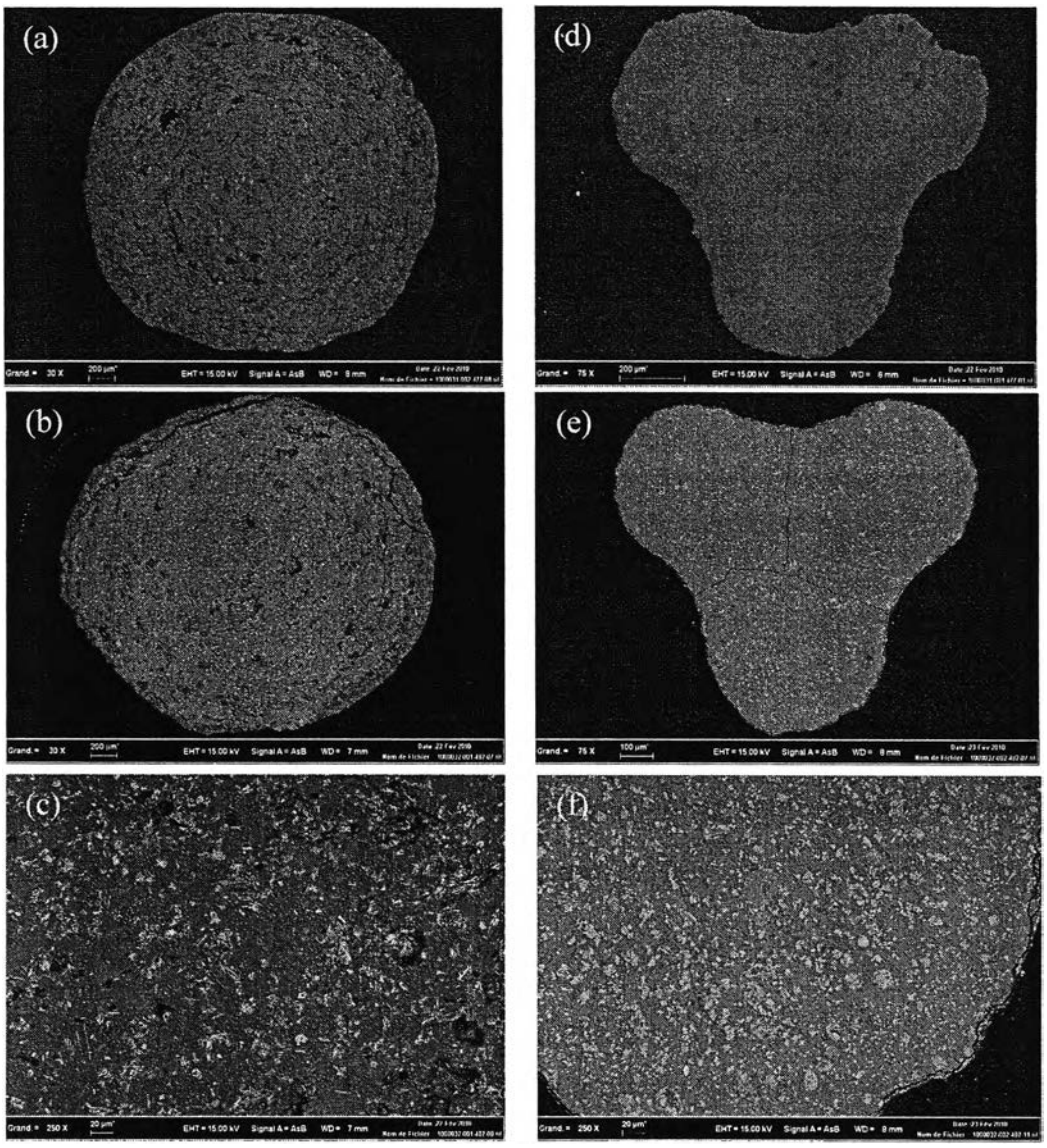

Figure 4.9 SEM images of surface and cross-section of adsorbents; (a) M-Al_2O_3 (×30), (b) 100 % monolayer of $CuCl_2$/M-Al_2O_3 (×30), (c) 100 % monolayer of $CuCl_2$/M-Al_2O_3 (×250), (d) m-Al_2O_3 (×75), (e) 100 % monolayer of $CuCl_2$/m-Al_2O_3 (×75) and (f) 100 % monolayer of $CuCl_2$/m-Al_2O_3 (×250).

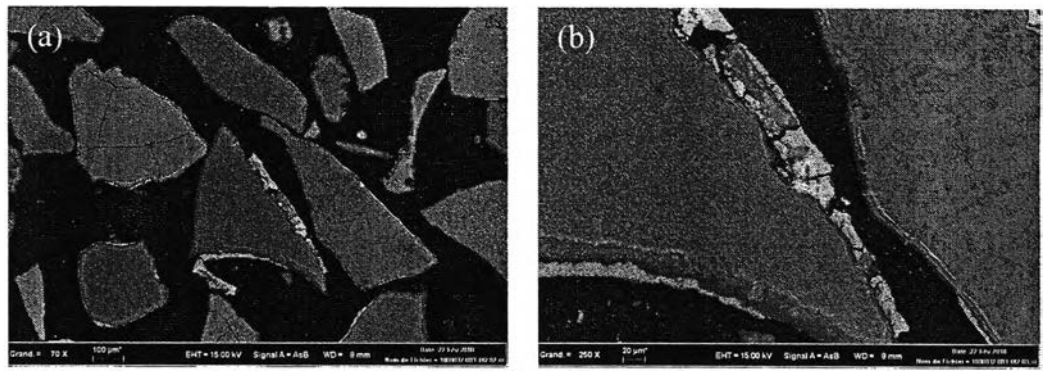

Figure 4.10 SEM images of surface and cross-section of small particle of 100% monolayer $CuCl_2$/m-Al_2O_3 crushed before impregnation at diameter size 300-500 μm; (a) (×70) and (b) (×250).

4.2 Fixed-Bed Adsorption Experiments

After activation of the adsorbent, the simulated diesel fuel feed (150 ppmw of S) was allowed to contact the bed and the total sulfur content in the effluent monitored periodically. The dead volume of the lines before and after the fixed-bed reactor was also determined in order to evaluate the cumulative effluent volume. The adsorption amounts were obtained after integrating the area above the breakthrough curves and below the line $C/C_0 = 1$. Breakthrough adsorption curves were generated by ploting the transient total sulfur concentration normalized by the feed total sulfur concentration versus cumulative eluted fuel volume.

4.2.1 Effect of Type of Adsorbents

The breakthrough experiments were performed at 0.4 cm^3/min and 30 °C, Figure 4.11 shows the sulfur breakthrough curves for simulated diesel fuel over non-impregnated activated carbon (AC), macroporous alumina (M-Al_2O_3), and mesoporous alumina (m-Al_2O_3) and Table 4.6 summarizes the results obtained for the breakthrough and adsorption capacities.

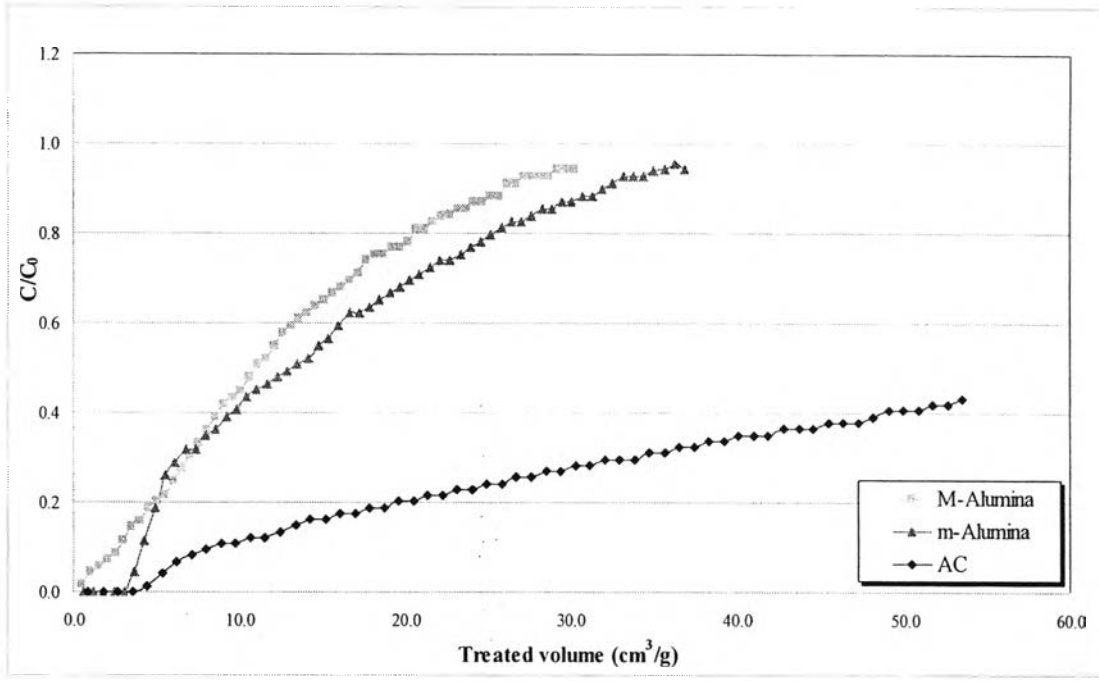

Figure 4.11 Breakthrough curve at of Dibenzothiophene in a fixed-bed adsorber at 0.4 cm^3/min and 30 °C over M-Al_2O_3 (▩),m-Al_2O_3 (▲) and AC (◆).

Table 4.6 Breakthrough and adsorption capacities loading for Dibenzothiophene from simulated diesel fuel in different non-impreganted adsorbents

Adsorbents	Adsorption capacity (mmol DBT/g Adsorbent)	Breakthrough capacity (mmol DBT/g Adsorbent)
M-Al_2O_3	0.0371	0.0015
m-Al_2O_3	0.0456	0.0097
AC	0.0824	0.0121

From Figure 4.11 and Table 4.6, the adsorption capacity increased in order of non-impregnated M-Al_2O_3 < non-impregnated m-Al_2O_3 < non-impregnated activated carbon, indicating that among the three different adsorbents, activated carbon has a highest efficiency which corresponds to the highest surface area. For the breakthrough capacity, corresponding to the capacity that leads to a purified effluent at 0 ppm, activated carbon is also higher than non-impregnated m-Al_2O_3 and M-Al_2O_3.

4.2.2 Effect of Feed Flow Rate

To study the effect of feed flow rate, which is related to the contact time allowing the sulfur compound in feed to be adsorbed on the surface of the adsorbent, the breakthrough experiments were performed at 2 and 0.4 cm^3/min and 30 °C. The results are shown in Figure 4.12 and Table 4.7.

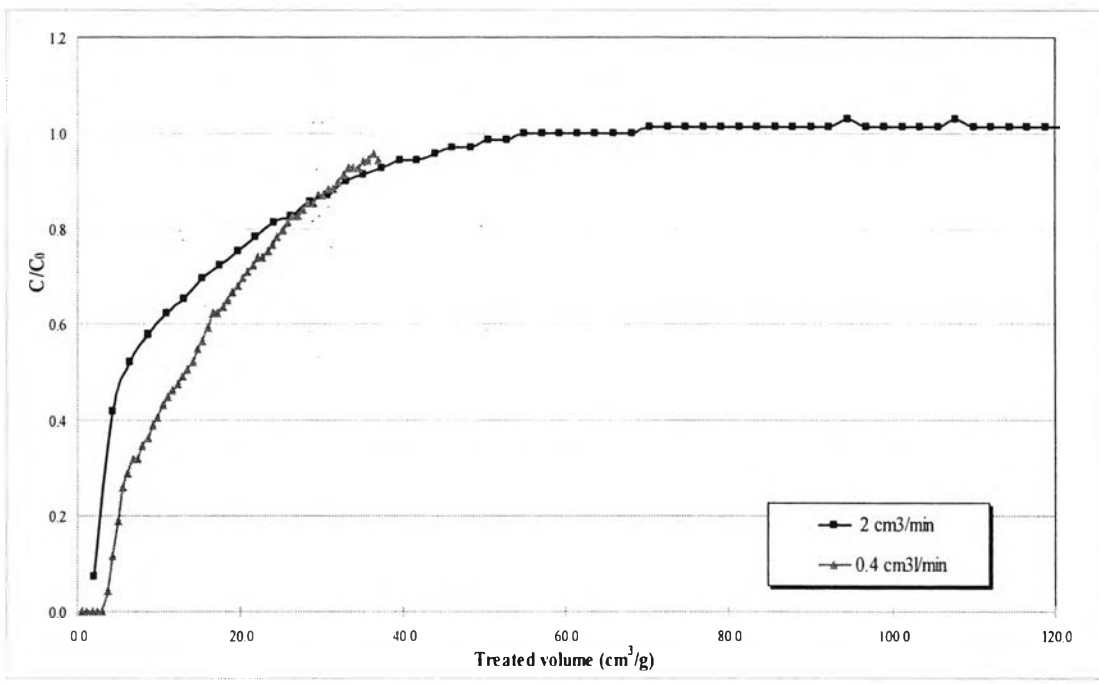

Figure 4.12 Breakthrough curve at of Dibenzothiophene in a fixed-bed adsorber at 30 °C over m-Al_2O_3 at feed flow rate 2 cm^3/min (■) and 0.4 cm^3/min (▲).

Table 4.7 Breakthrough and adsorption capacities loading for Dibenzothiophene from simulated diesel fuel in different feed flow rate

Flow rate	Adsorption capacity (mmol DBT/g Adsorbent)	Breakthrough capacity (mmol DBT/g Adsorbent)
2.0 cm^3/min	0.0482	0.0065
0.4 cm^3/min	0.0456	0.0097

From Figure 4.12 and Table 4.7, the lower feed flow rate at 0.4 cm^3/min showed the higher breakthrough capacity than the higher feed flow rate at 2.0 cm^3/min, as DBT had a greater contact time to be adsorbed on the surface and in then porosity of the adsorbent.

4.2.3 Effect of Adsorption Temperature

Since the kinetics of adsorption can be affected by adsorption temperature, the effect of adsorption temperature of mesoporous alumina was examined. The breakthrough experiments were studied at 30 °C and 90 °C at 0.4 cm^3/min of feed flow rate. The results are shown in Figure 4.13 and Table 4.8.

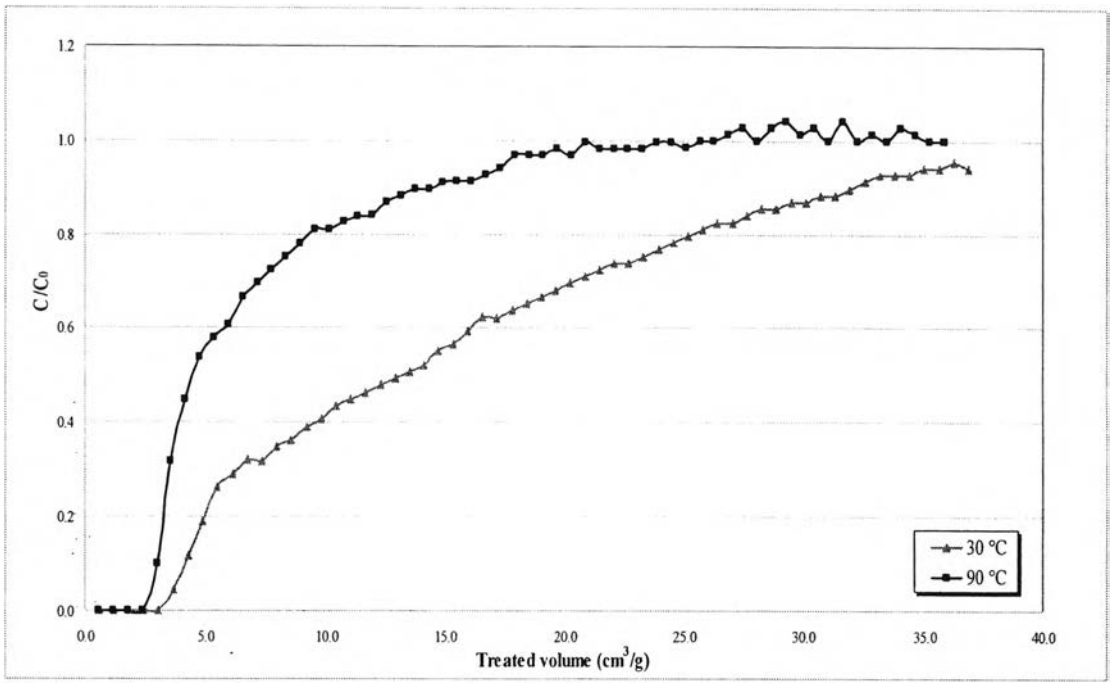

Figure 4.13 Breakthrough curve of Dibenzothiophene in a fixed-bed adsorber over m-Al_2O_3 at 0.4 cm^3/min by varying temperature; 30 °C (▲) and 90 °C (■).

Table 4.8 Breakthrough and adsorption capacities loading for Dibenzothiophene from simulated diesel fuel over activated carbon at different temperature

Temperature	Adsorption capacity (mmol DBT/g Adsorbent)	Breakthrough capacity (mmol DBT/g Adsorbent)
30 °C	0.0456	0.0097
90 °C	0.0246	0.0076

From Figures 4.13 and Table 4.8, the experiment at 30 °C showed a higher breakthrough capacity than at 90 °C, but at the higher temperature, the equilibrium is reached more rapidly. The kinetic effect was higher at high temperature, so DBT adsorbed rapidly and reached the equilibrium adsorption.

4.2.4 Effect of Amount of Metal Loading

To study the effect of amount of metal loading on the adsorbent, the experiments were carried out at at 0.4 cm^3/min and 30 °C. M-Al_2O_3 and m-Al_2O_3 impregnated by Cu^+ and Ni^{2+} at concentrations of 100%, 75% and 50% monolayer and AC impregnated by 43 wt% Cu^+ were used. The result are shown in Figures 4.14-4.4.18 and Table 4.9-4.13.

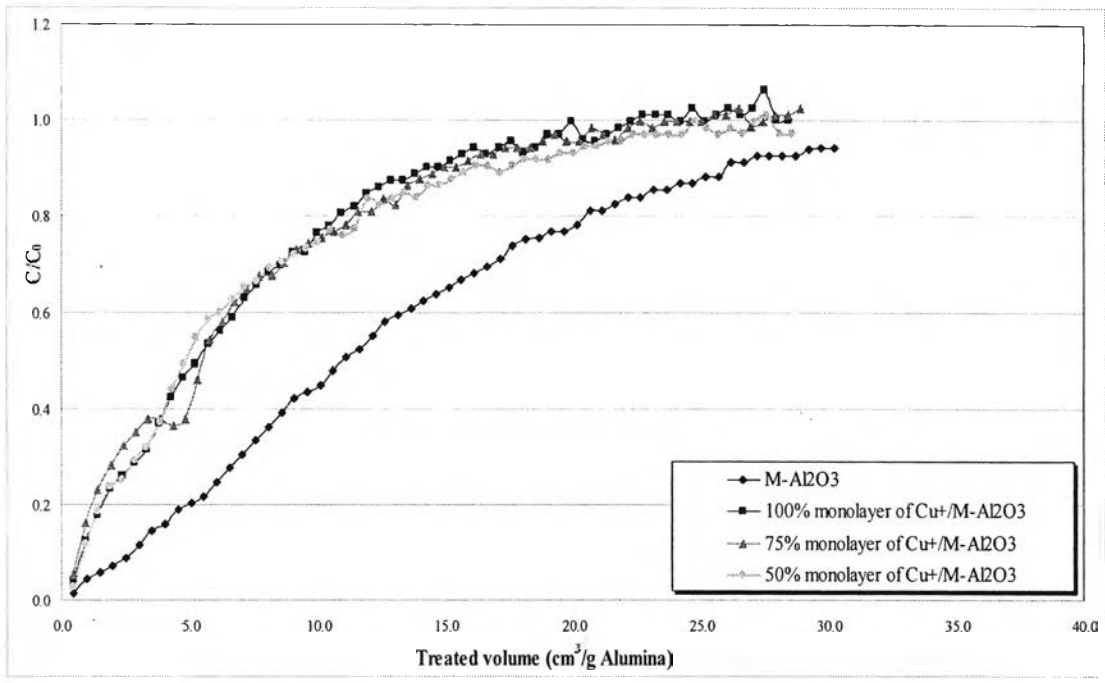

Figure 4.14 Breakthrough curve of Dibenzothiophene in a fixed-bed adsorber at 0.4 cm^3/min and 30 °C over M-Al_2O_3 (◆), 100% monolayer of Cu^+/M-Al_2O_3 (■), 75% monolayer of Cu^+/M-Al_2O_3 (▲) and 50% of monolayer Cu^+/M-Al_2O_3 (●).

Table 4.9 Breakthrough and adsorption capacities loading for Dibenzothiophene from simulated diesel fuel over M-Al_2O_3 at different amount of Cu^+ loading

% Cu^+ monolayer on M-Al_2O_3	Adsorption capacity (mmol DBT/g Adsorbent)	Breakthrough capacity (mmol DBT/g Adsorbent)
Non-impregnated	0.0371	0.0015
50%	0.0223	0.0014
75%	0.0208	0.0013
100%	0.0211	0.0012

The results of breakthrough experiments from M-Al_2O_3 at different amount of Cu^+ loading, non-impregnated, 100%, 75% and 50% monolayer, are shown in Figure 4.14 and Table 4.9.

From Figure 4.14, the results show that the metal seemed to decrease the adsorption capacity on M-Al_2O_3 while the amount of metal loading seemed to have no real effect, which is possible if there was too much Cu^+ as indicated by the SEM images showing agglomerates of $CuCl_2$.

And from Table 4.9, the adsorption capacity was decreased when impregnated by Cu^+ which corresponds to the lower porosity from nitrogen adsorption/desorption method and mercury. Breakthrough capacity was similar for all amount of Cu^+.

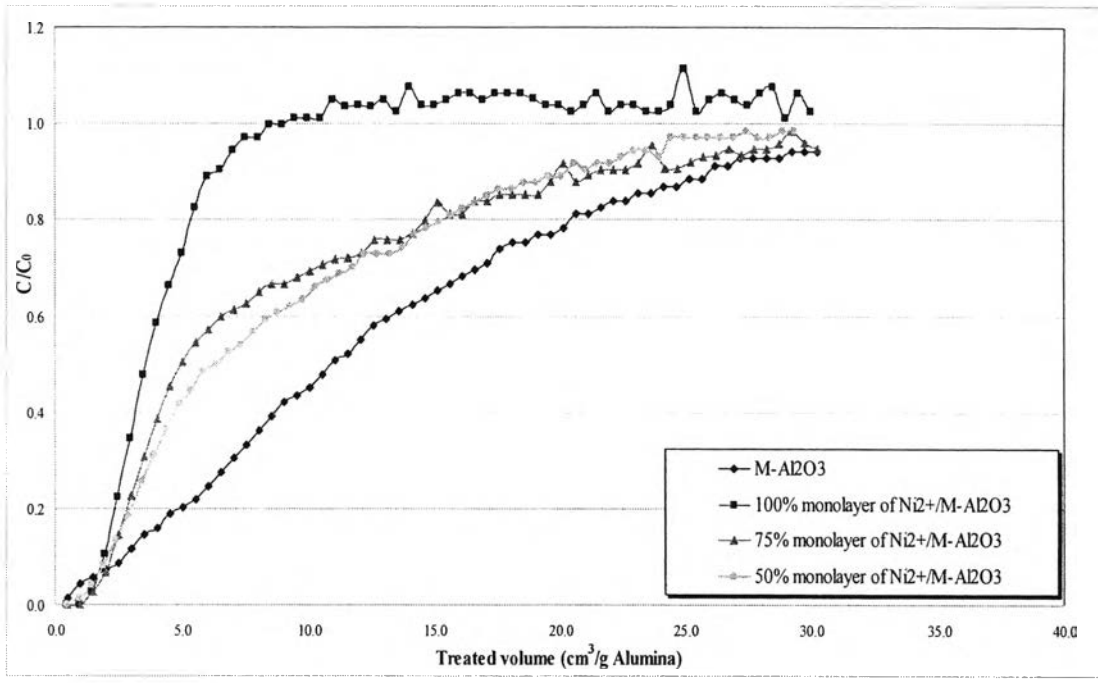

Figure 4.15 Breakthrough curve of Dibenzothiophene in a fixed-bed adsorber at 0.4 cm^3/min and 30 °C over M-Al_2O_3 (◆), 100% monolayer of Ni^{2+}/M-Al_2O_3 (■), 75% monolayer of Ni^{2+}/M-Al_2O_3 (▲) and 50% monolayer of Ni^{2+}/M-Al_2O_3 (●).

Table 4.10 Breakthrough and adsorption capacities loading for Dibenzothiophene from simulated diesel fuel over M-Al_2O_3 at different amount of Ni^{2+} loading

% Ni^{2+} monolayer on M-Al_2O_3	Adsorption capacity (mmol DBT/g Adsorbent)	Breakthrough capacity (mmol DBT/g Adsorbent)
Non-impregnated	0.0371	0.0015
50%	0.0283	0.0015
75%	0.0270	0.0032
100%	0.0179	0.0031

The results of breakthrough experiments from M-Al_2O_3 at different amount of Ni^{2+} loading, non-impregnated, 100%, 75% and 50% monolayer, are shown in Figure 4.15 and Table 4.10.

From Figure 4.15 and Table 4.10, the adsorption capacity was lower when the amount of Ni^{2+} loading was higher which corresponds to the lower porosity from nitrogen adsorption/desorption method and mercury porosimetry. Ni^{2+} seemed to increase the breakthrough capacity at concentration 75% and 100% monolayer, but for 50% monolayer, it was similar as the non-impregnated M-Al_2O_3.

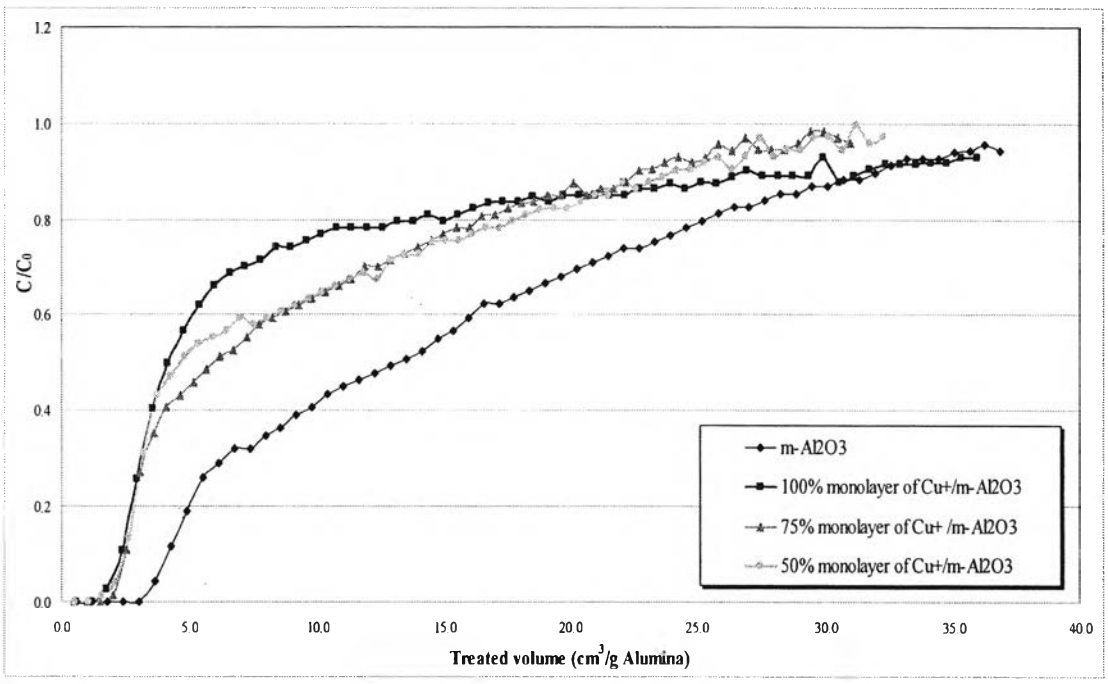

Figure 4.16 Breakthrough curve of Dibenzothiophene in a fixed-bed adsorber at 0.4 cm^3/min and 30 °C over m-Al_2O_3 (◆), 100% monolayer of Cu^+/m-Al_2O_3 (■), 75% monolayer of Cu^+/m-Al_2O_3 (▲) and 50% monolayer of Cu^+/m-Al_2O_3 (●).

Table 4.11 Breakthrough and adsorption capacities loading for Dibenzothiophene from simulated diesel fuel over m-Al_2O_3 at different amount of Cu^+ loading

% Cu^+ monolayer on m-Al_2O_3	Adsorption capacity (mmol DBT/g Adsorbent)	Breakthrough capacity (mmol DBT/g Adsorbent)
Non-impregnated	0.0456	0.0097
50%	0.0279	0.0031
75%	0.0248	0.0041
100%	0.0179	0.0030

The results of breakthrough experiments from m-Al_2O_3 at different amount of Cu^+ loading; non-impregnated, 100%, 75% and 50% monolayer are shown in Figure 4.16 and Table 4.11.

From Figure 4.16 and Table 4.11, the adsorption capacity was lower when the amount of Cu^+ loading was higher which corresponds to the lower porosity from nitrogen adsorption/desorption method and mercury porosimetry. At 75% monolayer, the higher breakthrough capacity is obtained, but still less than the non-impregnated m-Al_2O_3.

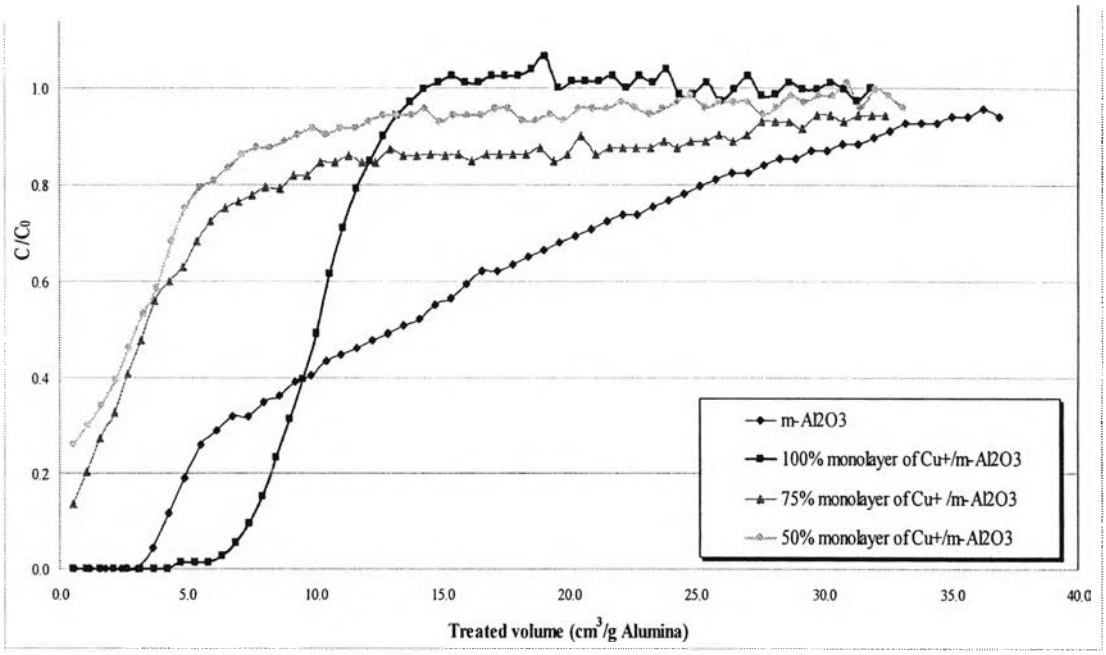

Figure 4.17 Breakthrough curve of Dibenzothiophene in a fixed-bed adsorber at 0.4 cm^3/min and 30 °C over m-Al_2O_3 crushed after impregnation at diameter size 300-500 μm; m-Al_2O_3 (◆), 100% monolayer of Cu^+/m-Al_2O_3 (■), 75% monolayer of Cu^+/m-Al_2O_3 (▲) and 50% of monolayer Cu^+/m-Al_2O_3 (●).

Table 4.12 Breakthrough and adsorption capacities loading for Dibenzothiophene from simulated diesel fuel over m-Al_2O_3 at different amount of Cu^+ loading at diameter size 300-500 μm and crushed after impregnation

% Cu^+ monolayer on m-Al_2O_3 (300-500 μm)	Adsorption capacity (mmol DBT/g Adsorbent)	Breakthrough capacity (mmol DBT/g Adsorbent)
Non-impregnated	0.0456	0.0097
50%	0.0139	0.0015
75%	0.0143	0.0014
100%	0.0278	0.0105

The results of breakthrough experiments from m-Al_2O_3 at different amount of Cu^+ loading, non-impregnated, 100%, 75% and 50% monolayer crushed after impregnation to be smaller at diameter size 300-500 μm, are shown in Figure 4.17 and Table 4.12.

From Figure 4.17 and Table 4.12, at 100% monolayer of Cu^+ showed the higher breakthrough capacity than non-impregnated, 50% and 75% monolayer of Cu^+, respectively. As alumina was crushed to small size, the external surface area was increased, so the adsorption was improved, but the results from 50% monolayer and 75% monolayer of Cu^+ was lower, so it need to study further. The adsorption capacity increased in oder of non-impregnated > 100% monolayer > 75% monolayer > 50% monolayer of Cu^+ because the metal decreased the surface area and porosity which corresponds to results from nitrogen adsorption/desorption method and mercury porosimetry.

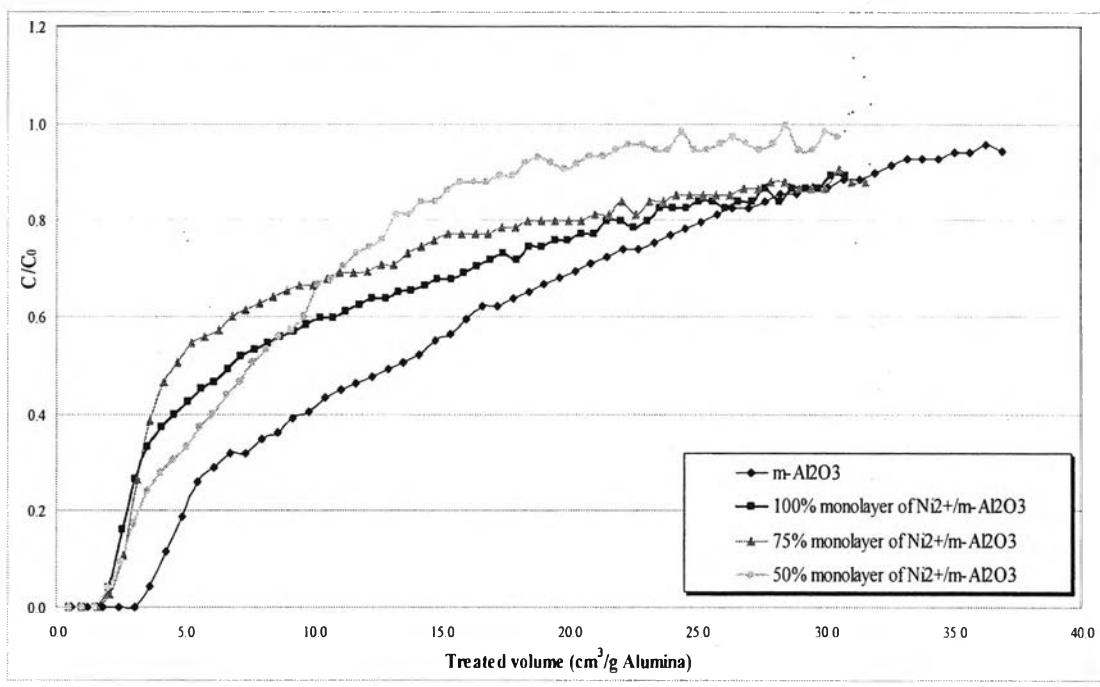

Figure 4.18 Breakthrough curve of Dibenzothiophene in a fixed-bed adsorber at 0.4 cm^3/min and 30 °C over m-Al_2O_3 (◆), 100% monolayer of Ni^{2+}/m-Al_2O_3 (■), 75% monolayer of Ni^{2+}/m-Al_2O_3 (▲) and 50% of monolayer Ni^{2+}/m-Al_2O_3 (●).

Table 4.13 Breakthrough and adsorption capacities loading for Dibenzothiophene from simulated diesel fuel over m-Al_2O_3 at different amount of Ni^{2+} loading

% Ni^{2+} monolayer on m-Al_2O_3	Adsorption capacity (mmol DBT/g Adsorbent)	Breakthrough capacity (mmol DBT/g Adsorbent)
Non-impregnated	0.0456	0.0097
50%	0.0291	0.0048
75%	0.0249	0.0048
100%	0.0278	0.0045

The results of breakthrough experiments from m-Al_2O_3 at different amount of Ni^{2+} loading, non-impregnated, 100%, 75% and 50% monolayer, are shown in Figure 4.18 and Table 4.13.

From Figure 4.18 and Table 4.13, the adsorption capacity was lower when the amount of Ni^{2+} loading was higher, which corresponds to the lower porosity from nitrogen adsorption/desorption method and mercury porosimetry. The breakthrough capacity was decreased when the metal was impregnated.

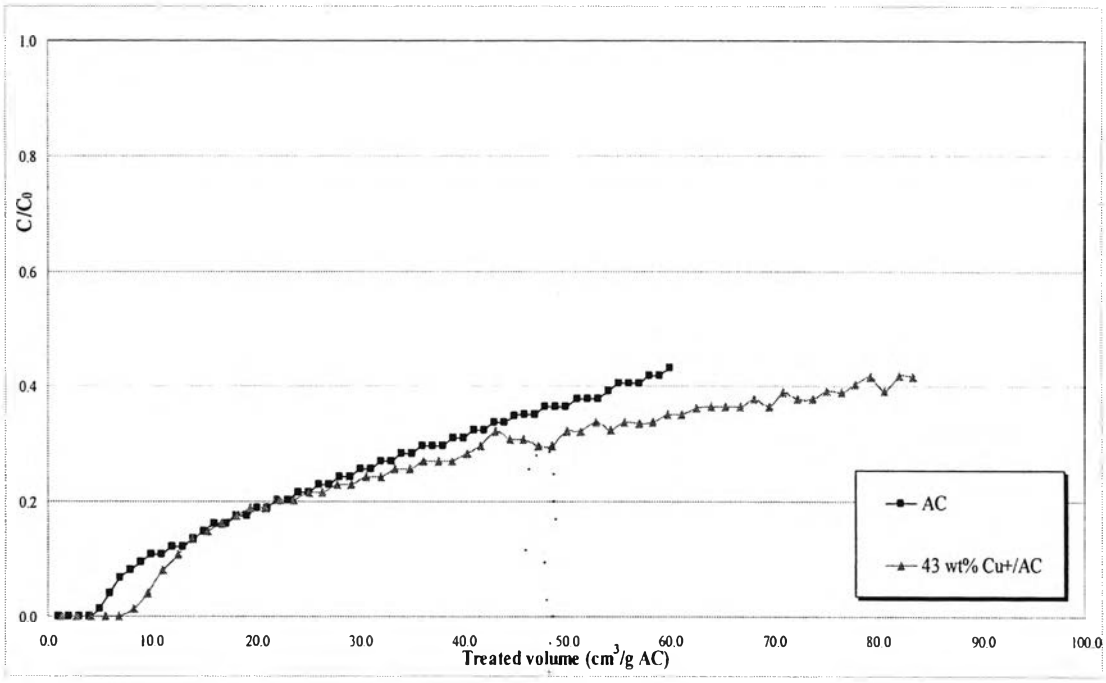

Figure 4.19 Breakthrough curve of Dibenzothiophene in a fixed-bed adsorber at 0.4 cm^3/min and 30 °C over AC (■) and 43% wt of Cu^+/AC (▲).

Table 4.14 Breakthrough and adsorption capacities loading for Dibenzothiophene from simulated diesel fuel over AC and 43 wt% of Cu^+ loading on AC.

Adsorbent	Adsorption capacity (mmol DBT/g Adsorbent)	Breakthrough capacity (mmol DBT/g Adsorbent)
AC	0.0824	0.0121
43% wt of Cu^+/AC	0.0627	0.0135

The results of breakthrough experiments from AC and 43%wt of Cu^+ impregnated on AC are shown in Figure 4.19 and Table 4.14.

From Figure 4.19 and Table 4.14, the adsorption capacity was lower when AC was impregnated by Cu^+, corresponding to the lower surface area and porosity from nitrogen adsorption/desorption method and mercury porosimetry. The breakthrough capacity of 43%wt of Cu^+ on AC was higher than with the non-impregnated AC indicating that Cu^+ increased the adsorption of sulfur.

4.2.5 Effect of Granulometry

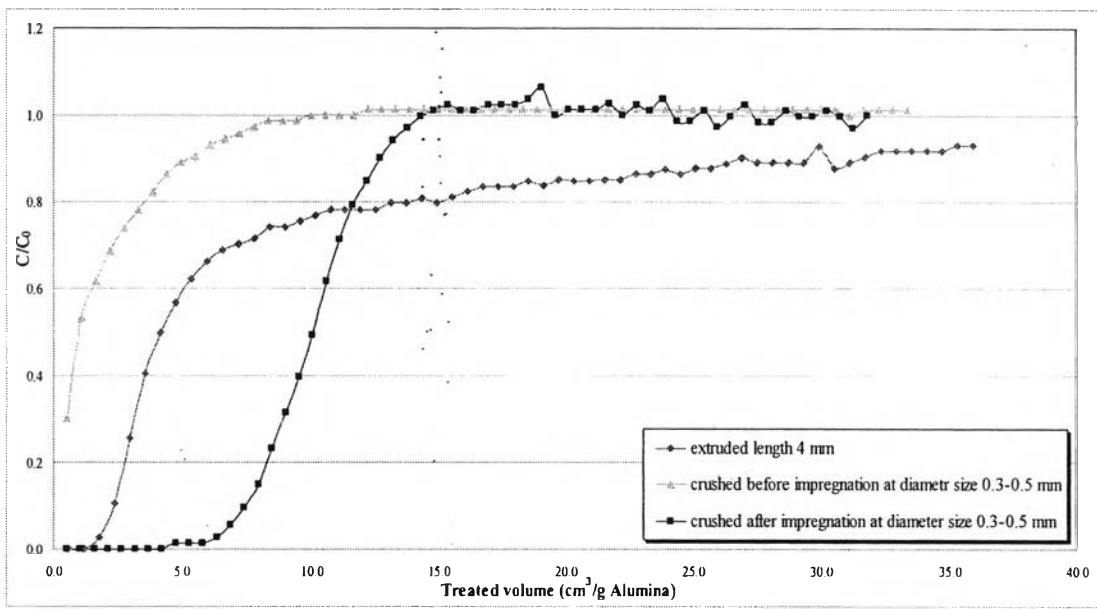

Figure 4.20 Breakthrough curve of Dibenzothiophene in a fixed-bed adsorber at 0.4 cm^3/min and 30 °C over different size and preparation of 100% monolayer of Cu^+/m-Al_2O_3; extruded length 4 mm (◆), crushed before impregnation at diameter size 300-500 μm (▲) and crushed after impregnation at diameter size 300-500 μm (■).

Table 4.15 Breakthrough and adsorption capacities loading for Dibenzothiophene from simulated diesel fuel over m-Al_2O_3 at different amount of Cu^+ loading

Size of 100% monolayer Cu^+ on m-Al_2O_3	Adsorption capacity (mmol DBT/g Adsorbent)	Breakthrough capacity (mmol DBT/g Adsorbent)
extruded length 4 mm	0.0179	0.0030
diameter size 300-500 μm which crushed before impregnation	0.0053	0.0013
diameter size 300-500 μm which crushed after impregnation	0.0278	0.0105

The results of breakthrough experiments from 100% monolayer of Cu^+ on m-Al_2O_3 at different size and preparation, extruded length 4 mm, crushed before impregnation at diameter size 300-500 μm and crushed after impregnation at diameter size 300-500 μm, are shown in Figure 4.20 and Table 4.15

From Figure 4.20 and Table 4.15, the results show that the smaller size at 300-500 μm diameter, crushed after impregnation, had the higher breakthrough and adsorption capacity than the 4 mm extruded length (normal size) and the 300-500 μm diameter, crushed before impregnation, respectively. In fact, the smaller adsorbent should be better, but according to the results from SEM, one can think that the metal covered mainly the external surface when crushing was done before impregnation, leading probably to a partial internal pore blocking, thus leading to a decrease in the adsorption efficiency.

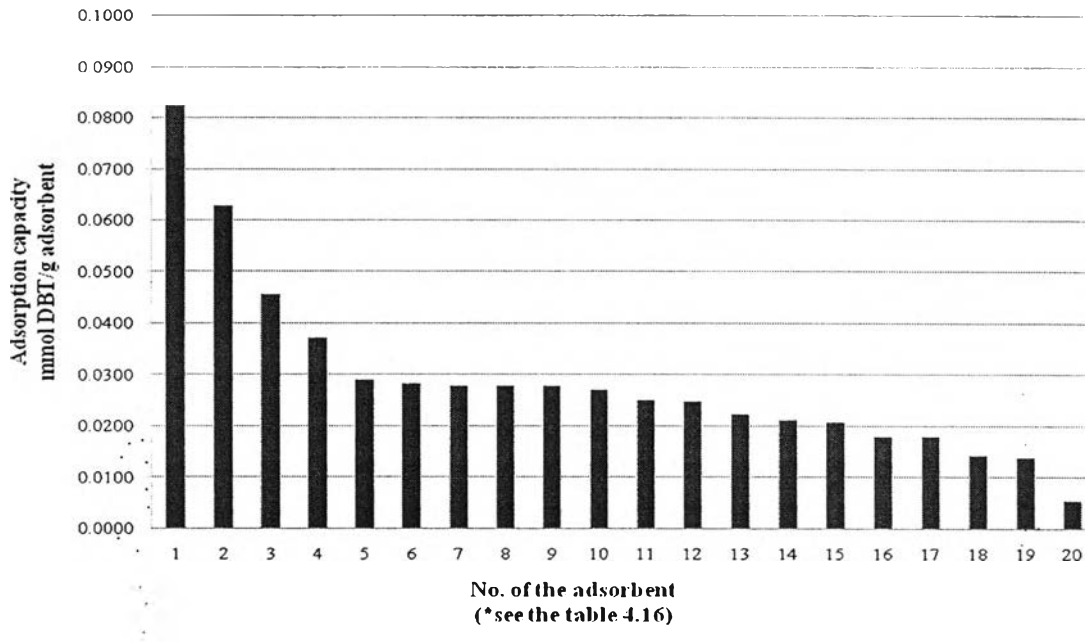

Figure 4.21 Summary graph of adsorption capacity of the all adsorbent in order of highest to lowest adsorption capacity at 0.4 cm^3/min and 30 °C.

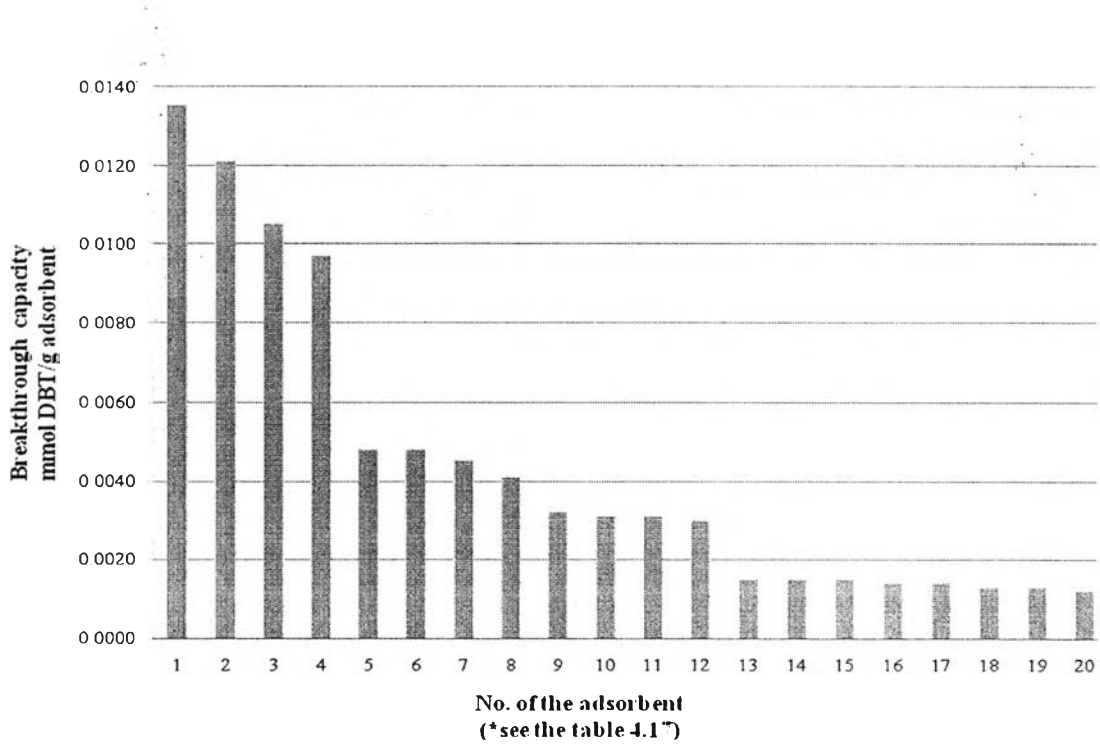

Figure 4.22 Summary graph of breakthrough capacity of the all adsorbent in order of highest to lowest adsorption capacity at 0.4 cm^3/min and 30 °C.

Table 4.16 Summary of the adsorption capacity of the all adsorbent at 0.4 cm^3/min and 30 °C

No. of the adsorbent	Adsorbent	Adsorption capacity (mmol DBT/ g Adsorbent)
1	Activated carbon	0.0824
2	43% wt of $CuCl_2$ on AC	0.0627
3	Mesoporous Alumina	0.0456
4	Macroporous Alumina	0.0371
5	50% monolayer of $NiCl_2$ on m-Al_2O_3	0.0291
6	50% monolayer of $NiCl_2$ on M-Al_2O_3	0.0283
7	50% monolayer of $CuCl_2$ on m-Al_2O_3	0.0279
8	Crushed *after* impregnation at diameter size 300-500 μm 100% monolayer of $CuCl_2$ on m-Al_2O_3	0.0278
9	100% monolayer of $NiCl_2$ on m-Al_2O_3	0.0278
10	75% monolayer of $NiCl_2$ on M-Al_2O_3	0.0270
11	75% monolayer of $NiCl_2$ on m-Al_2O_3	0.0249
12	75% monolayer of $CuCl_2$ on m-Al_2O_3	0.0248
13	50% monolayer of $CuCl_2$ on M-Al_2O_3	0.0223
14	100% monolayer of $CuCl_2$ on M-Al_2O_3	0.0211
15	75% monolayer of $CuCl_2$ on M-Al_2O_3	0.0208
16	100% monolayer of $NiCl_2$ on M-Al_2O_3	0.0179
17	100% monolayer of $CuCl_2$ on m-Al_2O_3	0.0179
18	Crushed *after* impregnation at diameter size 300-500 μm 75% monolayer of $CuCl_2$ on m-Al_2O_3	0.0143
19	Crushed *after* impregnation at diameter size 300-500 μm 50% monolayer of $CuCl_2$ on m-Al_2O_3	0.0139
20	Crushed before impregnation at diameter size 300-500 μm 100% monolayer of $CuCl_2$ on m-Al_2O_3	0.0053

Table 4.17 Summary of the breakthrough capacity of the all adsorbent at 0.4 cm^3/min and 30 °C

No. of the adsorbent	Adsorbent	Brekthrough capacity (mmol DBT/ g Adsorbent)
1	43% wt of $CuCl_2$ on AC	0.0135
2	Activated carbon	0.0121
3	Crushed *after* impregnation at diameter size 300-500 μm 100% monolayer of $CuCl_2$ on m-Al_2O_3	0.0105
4	Mesoporous Alumina	0.0097
5	50% monolayer of $NiCl_2$ on m-Al_2O_3	0.0048
6	75% monolayer of $NiCl_2$ on m-Al_2O_3	0.0048
7	100% monolayer of $NiCl_2$ on m-Al_2O_3	0.0045
8	75% monolayer of $CuCl_2$ on m-Al_2O_3	0.0041
9	75% monolayer of $NiCl_2$ on M-Al_2O_3	0.0032
10	50% monolayer of $CuCl_2$ on m-Al_2O_3	0.0031
11	100% monolayer of $NiCl_2$ on M-Al_2O_3	0.0031
12	100% monolayer of $CuCl_2$ on m-Al_2O_3	0.0030
13	Macroporous Alumina	0.0015
14	50% monolayer of $NiCl_2$ on M-Al_2O_3	0.0015
15	Crushed *after* impregnation at diameter size 300-500 μm 50% monolayer of $CuCl_2$ on m-Al_2O_3	0.0015
16	50% monolayer of $CuCl_2$ on M-Al_2O_3	0.0014
17	Crushed *after* impregnation at diameter size 300-500 μm 75% monolayer of $CuCl_2$ on m-Al_2O_3	0.0014
18	75% monolayer of $CuCl_2$ on M-Al_2O_3	0.0013
19	Crushed before impregnation at diameter size 300-500 μm 100% monolayer of $CuCl_2$ on m-Al_2O_3	0.0013
20	100% monolayer of $CuCl_2$ on m-Al_2O_3	0.0012

The summary of adsorption capacity is shown in Figure 4.21 and Table 4.16, the great adsortption capacity presented with non-impregnated adsorbent which corespond to the higher surface area while the lowest one was 100% monolayer of $CuCl_2$ on m-Al_2O_3 which crushed before impregnation at diameter size 300-500 μm which corespond to the result from SEM that the metal covered only external surface so internal surface seemed to be blocked then the efficiency was decreased.

The summary of breakthrough capacity is shown in Figure 4.22 and Table 4.17, the breakthroug capacity decreased in order of AC > 43% wt of $CuCl_2$ on AC > 100% monolayer of $CuCl_2$ on m-Al_2O_3 which crushed after impregnation at diameter size 300-500 μm > mesoporous alumina > 50% monolayer of $NiCl_2$ on m-Al_2O_3, respectively. AC showed the higher breakthrough capacity than the others because of the highest surface area while Ni^{2+} trended to increse the breakthrough capacity than Cu^{+}.